NUMERIAL STUDY OF VORTEX-INDUCED VIBRATION OF CIRCULAR CYLINDER ADJACENT TO PLANE BOUNDARY USING DIRECT-FORCING IMMERSED BOUNDARY METHOD

M. J. Chern*

Department of Mechanical Engineering
National Taiwan University of Science and Technology
Taipei, Taiwan

G. T. Lu **Y. H. Kuan** **S. Chakraborty**

Department of Mechanical Engineering
National Taiwan University of Science and Technology
Taipei, Taiwan

G. Nugroho

Department of Mechanical Engineering
Institute Teknologi Sepuluh Nopember
Surabaya, Indonesia

C. B. Liao

Department of Water Resources Engineering and Conservation
Feng Chia University
Taichung, Taiwan

T. L. Horng

Department of Applied Mathematics
Feng Chia University
Taichung, Taiwan

ABSTRACT

Vortex-induced vibration (VIV) is an important physical phenomenon as one design a riser or a cylindrical structure in ocean. As the riser or the cylindrical structure is adjacent to a seabed, the boundary effect on VIV is not fully understood yet. The direct-forcing immersed boundary (DFIB) method is used to investigate a two-degree-of-freedom VIV of a flexible supported circular cylinder adjacent to a plane boundary in this study. Furthermore, the effect of the VIV of cylinder on skin friction of the plane boundary is investigated. The effects of varying reduced velocity and gap ratio on VIV are discussed. Only a single vortex street is found when the cylinder is close to plane boundary. Hydrodynamic coefficients of the freely vibrating cylinder are analyzed in time and spectral domains. Furthermore, nearly round oval-shaped motion is observed as the so-called lock-in phenomenon occurs. The skin friction of the plane boundary is predicted by the DFIB model. Results show that the vibrating cylinder in the boundary layer flow can reduce the friction effectively. This proposed DFIB model can be useful for the investigation of VIV of the structures under the plane boundary effect even for a small gap between the cylinder and the boundary.

Keywords: Direct-forcing immersed boundary method, Vortex-induced vibration, Boundary layer flow, Lock-in.

* Corresponding author (mjchern@mail.ntust.edu.tw)

DOI : 10.1017/jmech.2017.55
Copyright © 2017 The Society of Theoretical and Applied Mechanics
Downloaded from https://www.cambridge.org/core. National Taiwan University, on 15 May 2018 at 01:02:41, subject to the Cambridge Core terms of use, available at https://www.cambridge.org/core/terms. https://doi.org/10.1017/jmech.2017.55

1. INTRODUCTION

Vortex-induced vibration (VIV) of structures is one of the important issue in ocean engineering. Vibration of a pipeline or a riser under water is a typical VIV example. VIV exists under the action of unsteady hydrodynamic forces arising from alternate vortex shedding behind a solid body immersed in fluid flow. As vortices shed, the periodic forces exert on the solid body in a flow field. Self-excited vibrations would be induced when the vortex-shedding frequency is close to its natural frequency. This is the so-called lock-in phenomenon. It is often to deploy those risers or cylindrical structures near the seabed. VIV is also found under the influence of the seabed. Details of VIV affected by the seabed is still not completely studied, so it is necessary to explore the effect of the seabed or a plane boundary on VIV as the risers or cylindrical structures are used above the seabed. Herein, a circular cylinder is considered as the cylindrical structure in ocean. The other issue of VIV of a cylinder adjacent to a plane boundary is its effect on friction of the boundary. Vortex-induced vibration of a circular cylinder near a solid structure such as an airfoil or another big cylinder can be used as a passive control method for drag reduction for the airfoil or the big cylinder [1]. The boundary layer flow above a rigid boundary is disturbed by the vibrating body and subsequently the friction drag over the rigid boundary is reduced. Strykowski and Sreenivasan [2] studied the vortex-shedding behind circular cylinders by a proper placement of a second, much smaller, cylinder in the near wake of the main cylinder. The other application reported by Igarashi [3] places a small circular cylinder upstream of the prism controlling the surface flow and the free shear layer that separates from the bluff body and effectively reduces drag. Huang and Mao [4] reported the study in a passive self-excited, transversely oscillating-rod technique for the separation control of the boundary layer on the cantilever wing. Their results reveal that VIV in the transverse direction can be used for modulation of surface flow. Yang *et al.* [5] undertook the experiments of a freely vibrating cylinder with single-degree-of-freedom and close to a rigid plane boundary in a flume. Their investigations showed that whether the small circular cylinder is fixed or vibrating, placing it near a solid boundary could significantly affect the surface flow and change the aerodynamic coefficient. All those technical papers indicate that the surface flow above a rigid boundary is affected by the vibrating circular cylinder above it. Apparently, the distribution of shear stress is changed and the resultant friction is reduced. The seabed may be also affected by the change of shear stress due to VIV of the adjacent risers or cylinder structures and its topography may be changed.

Numerical simulations for VIV have been conducted by a number of researchers. For example, Singh and Mittal [6] utilized the stabilized space-time finite-element method to simulate two degree-of-freedom (2DOF) VIVs of a circular cylinder. They predicted the lock-in phenomenon and hysteresis. 2S and P+S vortex-shedding modes were also shown and explained in their study. Dettmer and Perić [7] adopted the finite element method with an arbitrary Lagrangian-Eulerian (ALE) strategy to simulate the one-degree-of-freedom (1DOF) VIV of circular and rectangular cylinders. Responses of lock-in phenomena were successfully predicted. Du *et al.* [8] considered an elastically-mounted cylinder in compressible flow. An immersed boundary method was employed to solve 1DOF VIVs in the traverse direction. Three-dimensional flow variation due to VIV was shown and the P+S and 2P modes were found in the solutions. Chern *et al.* [9] undertook simulations for the 2DOF VIV. 2S and C(2S) vortex shedding modes were found in the 2DOF VIVs. The slightly oval and eight-shape trajectories in the lock-in region were predicted properly.

Despite VIV in a uniform current has been numerically solved by those researchers, it is a challenging issue as the vibrating cylinder close to a plane boundary. It is due to the narrow gap between the cylinder and the boundary. For those numerical methods using a boundary- fitted grid, it is difficult to use a very small and distorted grid to simulate the gap flow. Especially, when the cylinder vibrates above the boundary and almost touch the boundary, it becomes extremely arduous to utilize this distorted grids for simulations of the gap flow. Zhao and Cheng [10] gave numerical examples using the distorted grids and the ALE approach to simulate VIV of a cylinder above a plane boundary. To overcome the problem, an immersed boundary method which does not need a distorted grid for the complex solid geometry is used as an alternative numerical approach. An immersed boundary method simulates the solid motion using the Lagrangian frame but it solve the fluid flow in a fixed Cartesian grid. The main principle of an immersed boundary method is to use a virtual force in the momentum equations for the effect of solids on fluids. Grids in an immersed boundary method do not need to be distorted to fit the complex boundary or the moving boundary. Immersed boundary methods as reviewed by Sotiropoulos and Yang [11] have been considered as efficient numerical approaches for simulating complex fluid-structure interaction problems in the past two decades. For VIV simulations, Yang and Stern [12] developed a direct-forcing immersed boundary method to simulate 2DOF VIVs of a circular cylinder. Various trajectories of the cylinder were reported. The direct-forcing approach was proposed by Mohd. Yusof [13]. Du *et al.* [8] developed a three-dimensional immersed boundary model to predict 1DOF VIVs of a circular cylinder and observed vortex-shedding modes. In this study, a direct-forcing immersed boundary method (DFIB) is adopted for simulations of VIVs above a plane boundary. The DFIB methods was used for simulations of uniform flow past circular cylinders first [14]. DFIB simulation method has been preferred for its simplicity and robustness in resolving fluid structure interaction (FSI) situations. The DFIB method relies on a fixed Cartesian mesh, quite distinct from the conventional body-fitted routine, which uses an adaptive meshing method. The use of DFIB method eliminates the requirement of mesh regeneration at each time step. The

Downloaded from https://www.cambridge.org/core. National Taiwan University Library, on 15 May 2018 at 01:02:41, subject to the Cambridge Core terms of use, available at https://www.cambridge.org/core/terms. https://doi.org/10.1017/jmech.2017.55

import of this is the tremendous reduction in design time, which means a better turnaround. The novelty of the DFIB method, which is based on the momentum conservation principle, is anchored on the idea of replacing the solid body with its equivalent momentum effect on the equations governing the fluid motion. It has a great capability for handling complex geometries and moving bodies. Subsequently, Chern *et al.* [15] used this DFIB method to present the oscillatory flow past four cylindrical arrays. Variations of vortices around cylinders were observed and the influences on hydrodynamic loadings were presented. Moreover, Chern *et al.* [9] utilized the DFIB method to simulate the lock-in phenomena of 2DOF VIV of a circular cylinder in a uniform flow. Responses and vortex-shedding modes were depicted successfully.

In order to improve the problems mentioned above, the first explicit direct-forcing IB method was proposed by Uhlmann [16]. Uhlmann's method was further developed by Kempe and Fröhlich [17]. In this paper, the satisfaction of the velocity boundary conditions was improved by iterations. For the case of an implicit direct-forcing IB method, Wang and Zhang [18] developed a direct-forcing IB method based on the discrete stream function with local mesh refinement. To accommodate the interaction between a solid and a fluid flow, the body is identified by a volume-of solid function η which is reported by Noor *et al.* [14]. In order to facilitate the implementation of problems in complex flow simulations, the hybrid Cartesian-immersed boundary method was proposed by Mohd. Yusof [13], it is indicated that the immersed boundary method based on curvilinear background grids. Furthermore, Deng *et al.* [19] conducted the simulation of a flow pass stationary circular cylinder and a downstream elastic circular cylinder also use a hybrid Cartesian-immersed boundary method and have good agreement with other literatures.

In the present study, numerical simulations of a freely vibrating cylinder adjacent to a plane boundary are undertaken to investigate the effect of the boundary on VIV. When a circular cylinder is exposed to a flow field, periodic forces are exerted on the solid body when vortices shed behind the cylinder. Vibration of the cylinder in the boundary layer flow is numerically predicted. Modes of vortex shedding are discussed. Variation of shear stress distribution on the plane boundary is determined. The influence of the vibrating cylinder on the variation is discussed.

2. MATHEMATICAL FORMULAE AND NUMERICAL METHODS

We have proposed a numerical model which employs the direct-forcing immersed boundary (DFIB) method and the finite volume method in the present study. A virtual force is considered in the incompressible Navier-Stokes equations to simulate the fluid-structure interaction by the DFIB method. The DFIB method has been successfully used in various fluid-structure interaction (FSI) problems (see [9, 14-15]). More details about the DFIB method are described as follows.

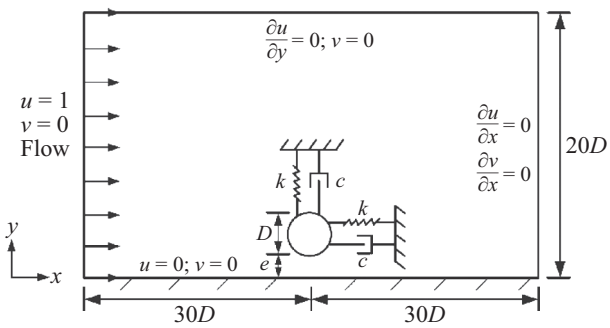

Fig. 1 Problem description and boundary conditions for VIV of an elastically mounted circular cylinder near a plane boundary.

2.1 Governing Equations and DFIB Method

A system of flow pass through an elastically mounted circular cylinder close to a plane boundary is illustrated in Fig. 1. Vortex shedding behind the circular cylinder allows it to vibrate in two degree-of-freedom (2DOF). The free stream is parallel to a plane boundary in the present study. In the present model, the distance between the inlet and the cylinder is enough to transform the free stream into a fully developed flow. The dimensionless governing equations of motion for an incompressible fluid flow can be expressed as

$$\nabla \cdot \mathbf{u} = 0, \tag{1}$$

and

$$\frac{\partial \mathbf{u}}{\partial t^*} + \nabla \cdot (\mathbf{u}\mathbf{u}) = -\nabla p + \frac{1}{Re}\nabla^2 \mathbf{u} + \mathbf{f}^*, \tag{2}$$

where $\mathbf{u}$ and p are non-dimensional velocity and pressure, respectively. $\mathbf{u}$ is non-dimensionalized by u_∞ which is the inlet free stream velocity, and p is a non-dimensionless pressure which is defined as $p^*/(\rho u_\infty^2)$, where p^* is the dimensional pressure and ρ is density of the fluid. Re is the Reynolds number defined by $u_\infty D/\nu$ where D is the cylinder diameter, ν is the kinematic viscosity of fluid, and $\mathbf{f}^*$ is the dimensionless virtual force term. In general, there are two different IB methods to handle complex geometries, one of them use a regular Eulerian computational grid for the fluid and a Lagrangian representation of the immersed boundary, which is first proposed by Peskin [20] (where the interaction between the fluid and the immersed elastic structure is expressed in terms of spreading and interpolation operations by use of smoothing Dirac delta functions), and the alternative IB method is the direct-forcing method proposed by Mohd. Yusof [13] and adopted in the present study. The forcing term $\mathbf{f}^*$ is defined as

$$\mathbf{f}^* = \eta \frac{\mathbf{u}_s - \mathbf{u}''}{\Delta t}, \tag{3}$$

and it can be defined by the difference between the interpolated velocity on the boundary point and the desired boundary velocity. Here, $\mathbf{u}_s$ and $\mathbf{u}''$ are denoted as the

Downloaded from https://www.cambridge.org/core. National Taiwan University Library, on 15 May 2018 at 01:02:41, subject to the Cambridge Core terms of use, available at https://www.cambridge.org/core/terms. https://doi.org/10.1017/jmech.2017.55

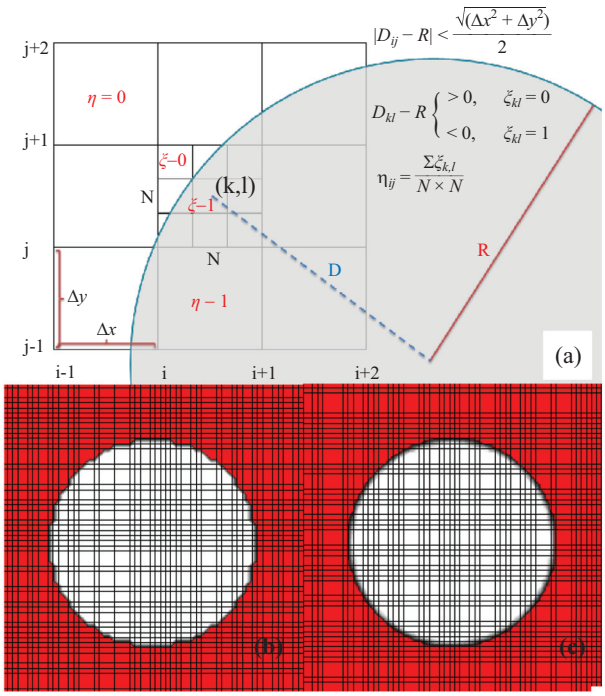

Fig. 2 Sub-grids use ξ to re-define the solid and fluid region: (a) volume-of-solid-function, (b) η contours without sub-grids, (c) η contours with sub-grids.

solid velocity of cylinder center and the second intermediate velocity. The solid body is identified by a volume-of-solid function, η, which denotes a fraction of solids within a cell where η is equal to 1 and 0 for solid and fluid cells, respectively, as reported by Noor *et al.* [14]. In order to implement a mesh refinement study in boundary cells, ξ is determined by Eq. (4) in each sub-grids. Therefore, the solid/fluid interface more closely resembles to smooth curves owing to dividing the main cells by setting the number of N, so the hydrodynamic coefficients can be resolved accurately. For an example, the circular cylinder is considered in the computational domain as shown in Fig. 2(a). Given that the distance between the center of the cylinder and the center of a sub-grid is less than the radius of the cylinder, then ξ will be 1. On the contrary, ξ is 0 when the distance is greater than radius.

$$\eta_{i,j} = \frac{\sum \xi_{k,l}}{N \times N'} \tag{4}$$

where k, l are the updated cell indices upon the determination of $\xi_{k,l}$ in each sub-cell by following Eq. (5);

$$\eta(x,y,t) = \begin{cases} 1, & (x - x_c(t))^2 + (y - y_c(t))^2 \le R^2 \\ 0, & (x - x_c(t))^2 + (y - y_c(t))^2 > R^2 \end{cases}, \tag{5}$$

where R is the radius of the cylinder, (x, y) are the coordinates of the center of the grid cell under consideration, and (x_c, y_c) are the coordinates of the cylinder [14]. Fig. 2(c) shows after the improvement, the solid boundary is smoother compared to the one before improvement showed in Fig. 2(b).

2.2 Equations of Motion for Vibrating Rigid Body

For the present VIV study, the moving structure is assumed to be rigid and mounted on elastic bases that allow displacements in the in-line and transverse directions. The equation of a mass-damper spring system forced by the hydrodynamic loading can be utilized to describe such behavior of a vibrating structure. According to the Newton's second law of motion, the velocity and the position of the cylinder center need to be computed from the instantaneous hydrodynamic forces that exert on a solid body. The motion of the solid body in the two dimensional Cartesian coordinate system is governed by the dimensionless equations as follows:

$$\ddot{X} + \frac{4\pi\zeta}{U_R^*}\dot{X} + \left(\frac{2\pi}{U_R^*}\right)^2 X = \frac{2C_D(t^*)}{\pi m^*}, \tag{6}$$

and

$$\ddot{Y} + \frac{4\pi\zeta}{U_R^*}\dot{Y} + \left(\frac{2\pi}{U_R^*}\right)^2 Y = \frac{2C_L(t^*)}{\pi m^*}, \tag{7}$$

where $\ddot{X}$, $\dot{X}$ and X are the normalized in-line acceleration, velocity and displacement of the center of a circular cylinder, respectively, while $\ddot{Y}$, $\dot{Y}$ and Y are in the transverse direction. $U_R^*\left(=\frac{u_\infty}{f_n D}\right)$, is the reduced velocity of the system, $f_n^*\left(=\frac{f_n D}{u_\infty}\right)$, is reduced natural frequency and the term $\zeta\left(=\frac{c}{2\sqrt{m_s k}}\right)$, is the structural damping ratio.

Downloaded from https://www.cambridge.org/core. National Taiwan University Library, on 15 May 2018 at 01:02:41, subject to the Cambridge Core terms of use, available at https://www.cambridge.org/core/terms. https://doi.org/10.1017/jmech.2017.55

The term $m^*\left(=\frac{4m_s}{\pi\rho_f D^2 L}\right)$, is the mass ratio of solid to liquid mass while $C_D(t^*)$ and $C_L(t^*)$ are the instantaneous drag and lift force coefficients, respectively defined in Eqs. (11) and (12). The fourth order Runge-Kutta algorithm is employed to solve Eqs. (6) and (7) after instantaneous C_D and C_L are determined at each time step. The diameter of cylinder D is defined as the characteristic length in the present work. The structural stiffness and the structural damping are assumed to be an isotropic in the study of two-degree-of-freedom vibrations.

2.3 Numerical Methods for Solving the Navier-Stokes Equations

The DFIB method uses a simple Cartesian grid to handle complex geometry problem. We employ the finite volume method in order to solve the Navier-Stokes equations in those grids. Therefore, the spatial and temporal discretization using a number of numerical schemes are discussed as follows.

Spatial and temporal discretizations: The second order central difference scheme and the third order quadratic upstream interpolation for convective kinetics (QUICK) scheme proposed by Leonard [21] are used to discretize the diffusive and the convective terms of Eq. (2) in this paper, respectively. A staggered grid is used in the present work. The Adam-Bashforth scheme is applied to the temporal terms. This scheme can guarantee the third order accuracy of time integral. By solving the advection-diffusion equations without the pressure gradient and the virtual force term, the first intermediate velocity u′ is calculated and denoted as

$$\mathbf{u}' = \mathbf{u}^n + \frac{\Delta t^*}{12}[23S^n - 16S^{n-1} + 5S^{n-2}], \tag{8}$$

where S includes the diffusive and convective terms of Eq. (2) at each time step. To predict the first intermediate velocity in Eq. (8), the third order Adam-Bashforth temporal scheme is implemented.

We have followed the same procedure prediction-correction for pressure-velocity as Chern *et al.* [9] and Chern *et al.* [15] and solved the Poisson equation

$$\nabla^2 p^{n+1} = \frac{1}{\Delta t^*}\nabla\cdot\mathbf{u}', \tag{9}$$

by using the SOLA algorithm proposed by Hirt *et al.* [22]. In present study, the integral of the virtual force is the dimensionless resultant force exerted on a circular cylinder by using the Simpson's 1/3 rule.

$$\mathbf{F} = \iiint_\Omega \mathbf{f}^* \mathrm{d}V, \tag{10}$$

where $\mathbf{F}$ are the resultant of total dimensionless virtual forces. The dimensionless in-line and transverse force coefficients, C_D and C_L can be denoted as

$$C_D = -2F_x\left(=-\frac{R_x}{\frac{1}{2}\rho D u_\infty^2}\right), \tag{11}$$

and

$$C_L = -2F_y\left(=-\frac{R_y}{\frac{1}{2}\rho D u_\infty^2}\right), \tag{12}$$

where R_x and R_y are the dimensional resultant drag and lift. The time average of in-line and root-mean-square value of transverse forces in dimensionless form are defined as

$$\bar{C}_D = \frac{1}{t}\int_0^t C_D \mathrm{d}t, \tag{13}$$

and

$$C_{L,rms} = \left(\frac{1}{t}\int_0^t C_L^2 \mathrm{d}t\right)^{1/2}, \tag{14}$$

respectively. The skin-friction coefficient of a plane boundary is defined as

$$C_f = \frac{\tau_w}{\frac{1}{2}\rho u_\infty^2}, \tag{15}$$

Where $\tau_w\left(=\mu\frac{du}{dy}\right)$ is shear stress at the surface of a plane boundary, μ is dynamic viscosity. The time average of skin-friction coefficient of a plane boundary and the integral of skin-friction coefficient are defined as

$$\bar{C}_f = \frac{1}{T}\int_0^T C_f \mathrm{d}t, \tag{16}$$

and

$$\bar{C}_F = \int_0^L \bar{C}_f \mathrm{d}x, \tag{17}$$

where T is the time of the cylinder run in a cycle, L is the length of the plane boundary. The skin-friction drag reduction in percentage can be presented as

$$\gamma = \left(1 - \frac{\bar{C}_F}{\bar{C}_{F_0}}\right)\times 100\%, \tag{18}$$

where $\bar{C}_{F_0}$ is the skin-friction drag of a plane boundary without a cylinder. The higher γ indicates that the mechanisms of the drag reduction have a best performance.

2.4 Numerical Procedures for Fluid-Structure Interaction

Figure 3 shows the complete numerical procedures for fluid-structure interaction of the proposed DFIB method at each time step and it is summarized in the following algorithm.

1. Identify the immersed boundary location and determine the volume-of-solid function η at each cell.
2. Compute the first intermediate velocity $\mathbf{u}'$ by Eq.

Downloaded from https://www.cambridge.org/core. National Taiwan University Library, on 15 May 2018 at 01:02:41, subject to the Cambridge Core terms of use, available at https://www.cambridge.org/core/terms. https://doi.org/10.1017/jmech.2017.55

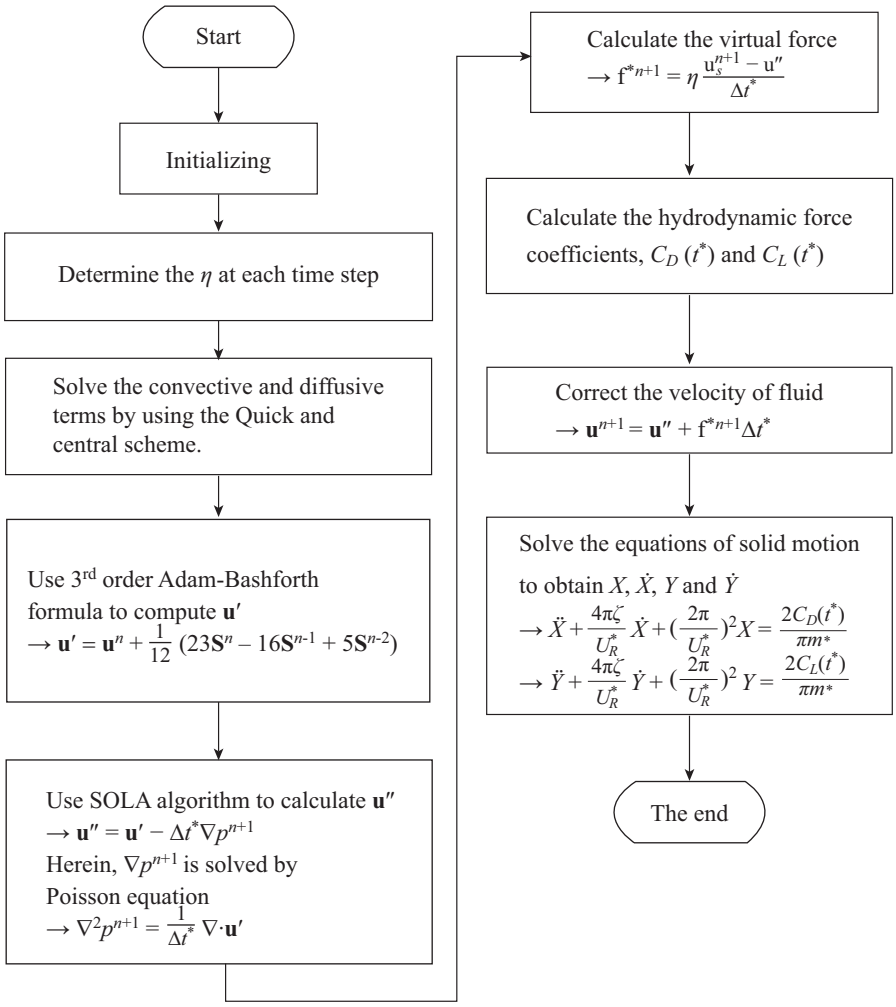

Fig. 3 Flow chart of numerical procedures for each time step.

(8) including the diffusive and convective terms.

3. Reconstruct the pressure gradient by solving the Poisson equation associated with Eq. (9), then advance the intermediate velocity $\mathbf{u}''$ by Eq. (8) in Chern *et al.* [9], to satisfy the mass conservation.

4. Solve the virtual force in the entire domain by means of Eq. (15) in Chern *et al.* [9]. Thus, the total hydrodynamic force acting on the solid, the drag and lift coefficients can be obtained from the Eqs. (10), (11) and (12), respectively.

5. Update flow field velocity $\mathbf{u}^{n+1}$ using the calculated virtual force by Eq. (12) in Chern *et al.* [9].

6. Calculate the solid motion described in Eqs. (6) and (7) to get the velocity and displacement of solid. If the solid is fixed, then $\mathbf{u}_s$ will be always zero.

2.5 Computational Domain and Computing Time

The computational domain of $60D \times 20D$ for simulations of a 2-DOF VIV problem where a circular cylinder adjacent to a rigid boundary, is discretized into $I \times J = 445 \times 223$ non-uniform grids as presented in Fig. 4. The purpose of using a non-uniform grid configuration is to increase the accuracy of the present method and to enhance the capturing of the VIV phenomenon. According to Chern *et al.* [9], DFIB modeling of VIV of a circular cylinder was completely certificated and has good result. The minimum grid size of $\Delta x = \Delta y = 0.025$ is employed in the vicinity of the vibrating cylinder. A time increment of $\Delta t^* = 10^{-3}$ satisfies the CFL condition. Herein, CFL number defined as $\left(\frac{u\Delta t}{\Delta x} + \frac{v\Delta t}{\Delta y}\right)$, is always less than 0.1 in the present study. The convergence criterion $\text{Đ} = 10^{-4}$ for the maximum mass residual is con-

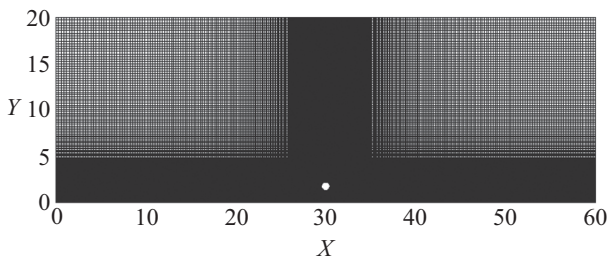

Fig. 4 The grid configurations for VIV of an elastically mounted circular cylinder adjacent to a plane boundary.

Downloaded from https://www.cambridge.org/core. National Taiwan University Library, on 15 May 2018 at 01:02:41, subject to the Cambridge Core terms of use, available at https://www.cambridge.org/core/terms. https://doi.org/10.1017/jmech.2017.55

sidered in this study. The longest simulation takes about 50 days, corresponding with the dimensionless run time $t^* = 800$. A PC cluster consisting of Intel Xeon E5-2697 v2 2.70 GHz CPUs is used to model the motion of 2-DOF cylinders.

2.6 Grid Independence and Validation of in-House Numerical Code

The numerical study of an uniform flow past a stationary cylinder using the current DFIB method at Re = 40 and 100 was successfully performed by Noor *et al.* [14]. The time history of recirculation length at $Re = 40$, $\bar{C}_D$ and St of the cylinder at $Re = 100$ have good agreement with other literatures in their results. Chern *et al.* [15] and Chern *et al.* [9] used the same DFIB method in the numerical prediction of cylinder array in oscillatory flow and vortex-induced vibration of a circular cylinder. Several grid configurations are utilized to simulate the transverse oscillations of a circular cylinder in order to ensure that the numerical results are grid independent especially for free vibrations of a circular cylinder. The flow and structural parameters are chosen according to Leontini *et al.* [23] using $Re = 200$, $m^* = 10$, $\zeta = 0.01$ and $U_R^* = 3.5$ in grid independent study. It is interesting to investigate the influence of the grid from the flow evolution since the proposed model is established for an unsteady flow. Based on the study of Chern *et al.* [9], there are four various corresponding smallest grid spacing of these meshes (0.1D, 0.05D, 0.025D and 0.020D) allocated in the vicinity of the cylinder. The time histories of the normalized transverse displacement given by $\Delta x = \Delta y = 0.025$ and 0.02 are very similar and overlapped with each other. The grid spacing $\Delta x = \Delta y = 0.025$ in the vicinity of the vibrating cylinder is adopted in present work to get more accuracy numerical results and to save the computational time. Herein, a total number of 1257 uniform grid cells are used to describe the vibrating cylinder.

3. RESULTS AND DISCUSSIONS

3.1 In-Line and Transverse Vibrations near a Plane Boundary

The dynamic responses of VIV of a circular cylinder adjacent to a plane boundary are investigated numerically in this simulation. The elastically mounted circular cylinder can oscillate in both transverse and stream wise directions. The parameters used in the present simulations are same as mentioned in the previous published (see [9]), however, $Re = 100$ and U_R^* alters in an interval between 4 and 12. The natural frequency of the structure is used to adjust the variation of U_R^*. In order to obtain the maximum amplitude, the value taken for the term m^* is 10 and ζ is set to 0. Herein, four different values of gap ratio, e which is normalized by D, are considered, such as 0.35, 0.6, 0.8 and 1.25 to investigate the influences of boundary layer on the vibrating cylinder.

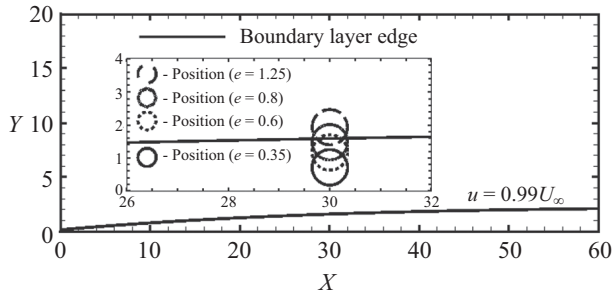

Fig. 5 Illustration of a circular cylinder in the boundary layer. The cylinder is located at $X = 30$. The gap ratios, e, 0.35, 0.6, 0.8 and 1.25, are considered in this study.

The calculated thickness of the boundary layer δ at Re = 100 is about 1.58D depending on free stream velocity, u_∞, cylinder diameter D and kinetic viscosity of fluid, ν. In Fig. 5, the effect of boundary layer on different positions, e = 0.35, 0.6, 0.8 and 1.25 are illustrated. We have taken care that the cylinder would not hit the rigid plane boundary due to the maximum amplitude in cases of e = 0.35, 0.6, 0.8 and 1.25. A parametric study is performed to investigate the effects of U_R^* and e on the amplitude and frequency responses of the vibrating cylinder.

3.2 Flow Patterns and Modes of Vortex Shedding

Figure 6 shows the time history of the normalized in-line and transverse displacements of the vibrating cylinder with e = 0.35, 0.6, 0.8, and 1.25. The monotonically periodic growing amplitude with e = 0.35, 0.6, 0.8, and 1.25 could be observed after it reaches the periodic state. Figure 6 also shows that the oscillation amplitudes in the transverse direction are greater than the in-line direction with the effect of boundary layer. Bearman and Zdravkovich [24] and Lei *et al.* [25] observed that the vortex shedding was suppressed at $e \leq 0.3$. The vortex shedding is affected by the plane boundary and the phenomenon of vortex shedding from the stationary cylinder vanishes when e decreases to a certain value.

The major vortex patterns near the fundamental lock-in region are 2S, 2P and P+S [26]. The designation 2S means that in each half cycle a vortex is fed into the downstream wake, 2P means the formation of vortex pairs which convect laterally outwards from the wake centerline, and the P+S mode is an asymmetric version of the 2P mode where the cylinder sheds a pair and a single vortex each cycle. Other patterns are denoted as C(2S) and C(P+S) which mean that near the cylinder, we have the 2S or P+S modes but the smaller vortices coalesce behind the solid body. Initially, the 2S mode appears near the wake and as gradually Reynolds number increases, different wake patterns similar to 2P and P+S modes appears. Plenty of results have been published previously for different flows involving an oscillating body and confirmed the similar wake patterns near the oscillating body.

Downloaded from https://www.cambridge.org/core. National Taiwan University Library, on 15 May 2018 at 01:02:41, subject to the Cambridge Core terms of use, available at https://www.cambridge.org/core/terms. https://doi.org/10.1017/jmech.2017.55

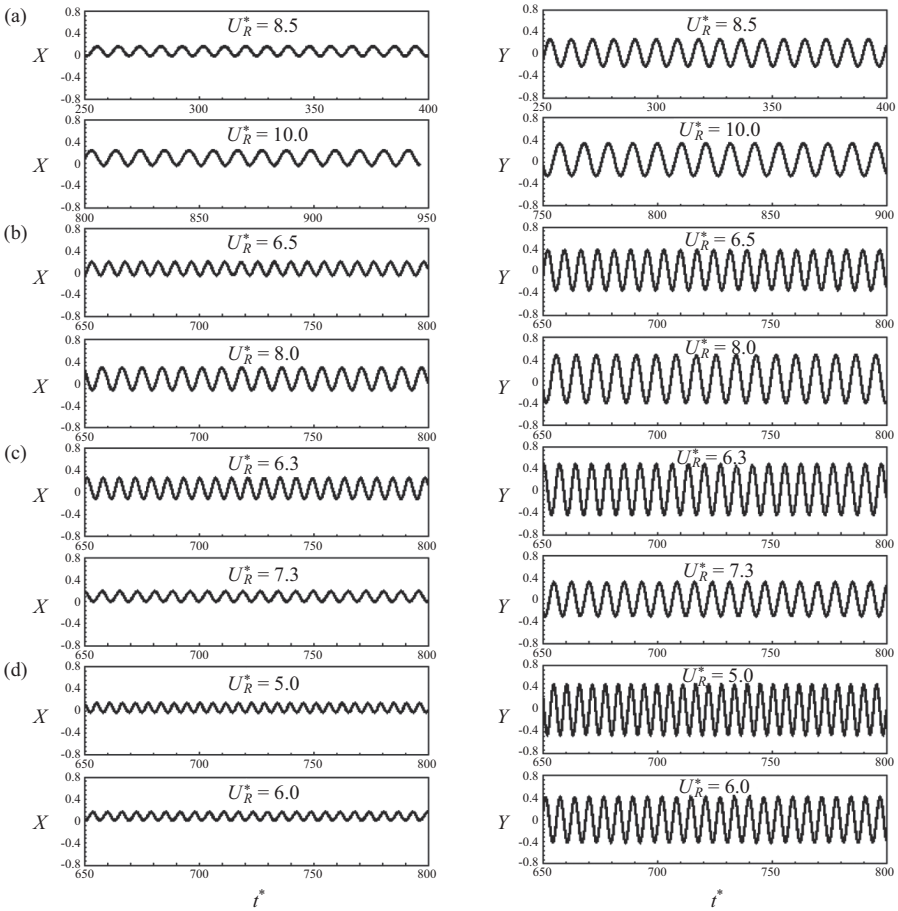

Fig. 6 Time histories of the normalized in-line and transverse displacements of vibrating cylinder adjacent to a plane boundary for different gap ratios when lock-in occurs: (a) $e = 0.35$, (b) $e = 0.6$, (c) $e = 0.8$, and (d) $e = 1.25$.

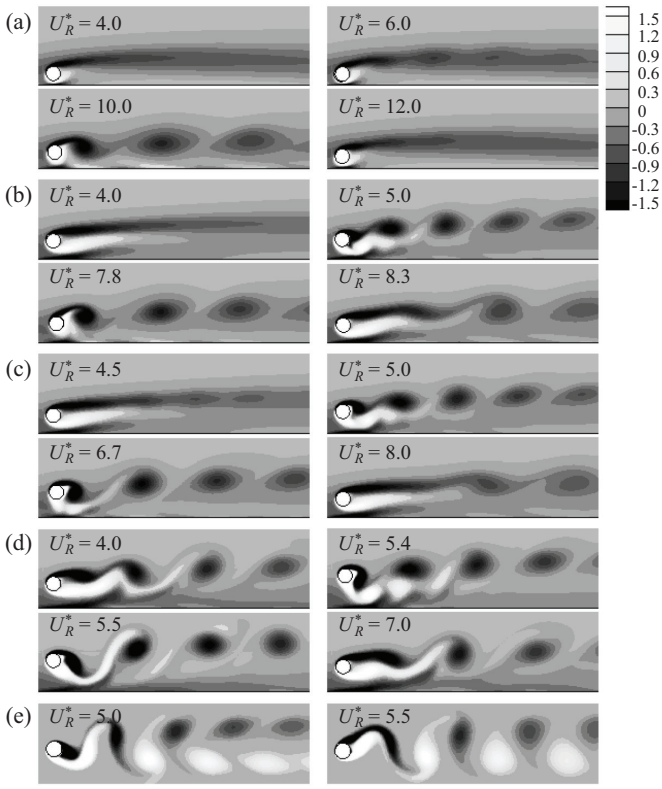

Fig. 7 Vortex shedding modes of vibrating cylinder adjacent to a plane boundary for different gap ratios: (a) $e = 0.35$, (b) $e = 0.6$, (c) $e = 0.8$, (d) $e = 1.25$, (e) $U_R^* = 5.0$ and $U_R^* = 5.5$, without a plane boundary.

Downloaded from https://www.cambridge.org/core. National Taiwan University Library, on 15 May 2018 at 01:02:41, subject to the Cambridge Core terms of use, available at https://www.cambridge.org/core/terms. https://doi.org/10.1017/jmech.2017.55

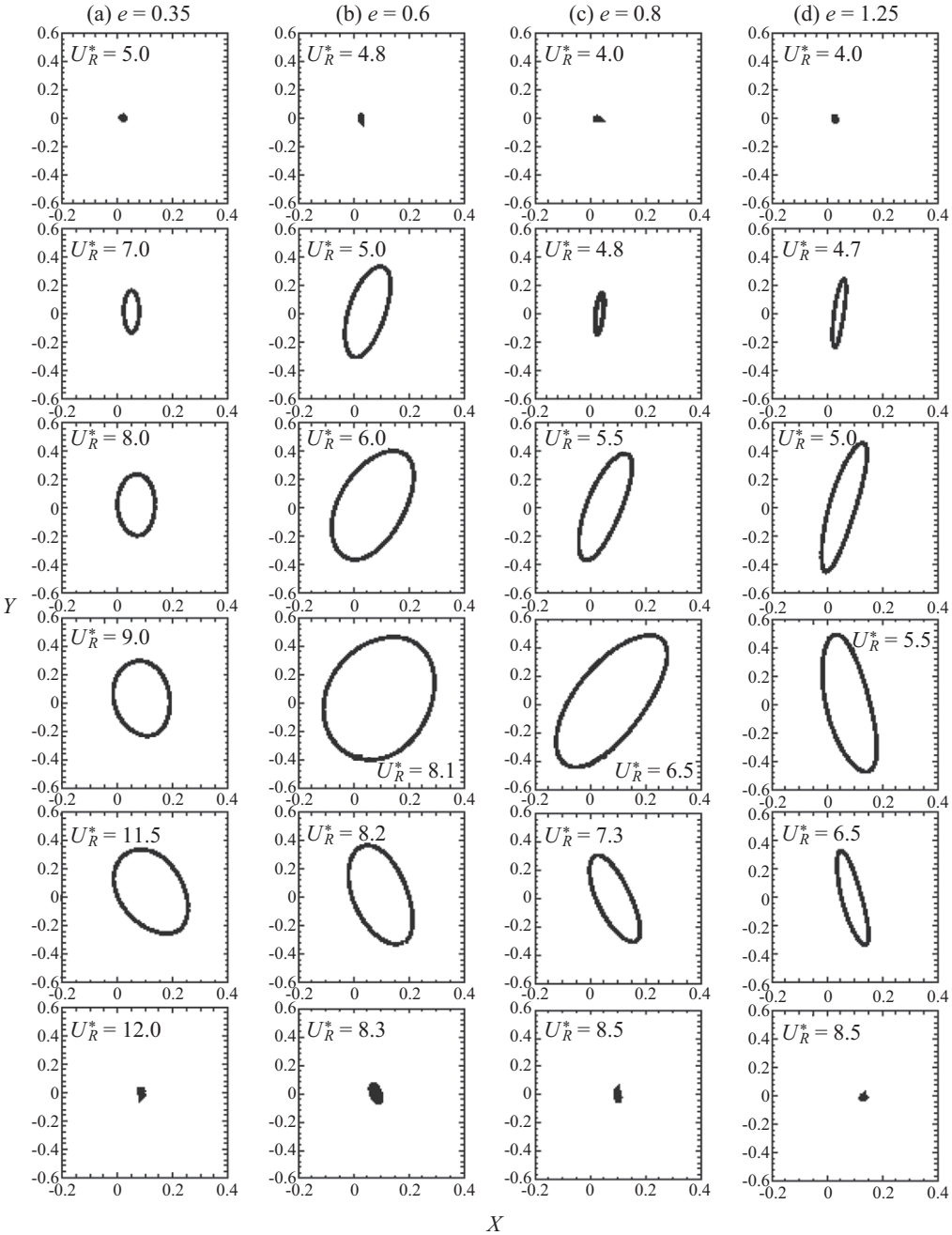

Fig. 8 Trajectory diagrams of the movement of vibrating cylinder adjacent to a plane boundary for different gap ratios: (a) $e = 0.35$, (b) $e = 0.6$, (c) $e = 0.8$, and (d) $e = 1.25$.

Figure 7 presents the flow visualization of wake flow around a two-degree-of-freedom circular cylinder with (a) $e = 0.35$, (b) $e = 0.6$, (c) $e = 0.8$, (d) $e = 1.25$ and (e) $U_R^* = 5.0$, $U_R^* = 5.5$, without a plane boundary where vortex shedding modes C(2S) and 2S are observed respectively. According to Williamson and Roshko [26], the 2S means that two single vortices are formed in each cycle and released from the cylinder. Moreover, C(2S) is similar to a 2S mode but vortices are coalesced in the wake behind the solid body. As shown in the figure, the vortices are shedding only from the top of the cylinder and the single clockwise vortex street dominates the wake process. Figures 7(a) $U_R^* = 4.0$, (b) $U_R^* = 4.0$ and (c) $U_R^* = 4.5$ presents that the separation occurs on the cylinder initially, but the size of the separation bubble is very small and it coalesces together due to the weak aerodynamic forces. In Fig. 7(d), clockwise vortex is stronger than Figs. 7 (a)-(c) because the cylinder is farther away from the plane boundary when $e = 1.25$, it is noted that single clockwise vortex shedding over the cylinder is found when $U_R^* = 4.0$. When it comes to the case without the effect of boundary layer which is studied by Chern *et al.* [9], the flow induced two-degree-of-freedom vibration of a circular cylinder in the uniform flow without a plane boundary at $Re = 100$, $m^* = 10$ and $\zeta = 0$ was investigated. Results show that

Downloaded from https://www.cambridge.org/core. National Taiwan University Library, on 15 May 2018 at 01:02:41, subject to the Cambridge Core terms of use, available at https://www.cambridge.org/core/terms. https://doi.org/10.1017/jmech.2017.55

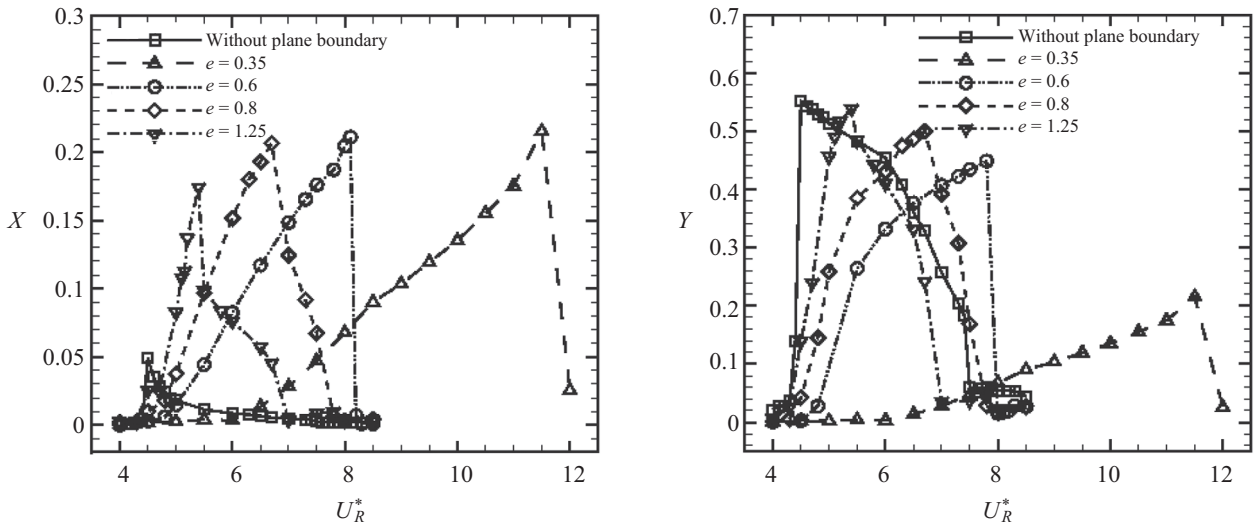

Fig. 9 Variation of values of maximum in-line and transverse displacements of vibrating cylinder with a variety of gap ratios and reduced velocities.

the C(2S) mode is discovered from $U_R^* = 4.5$ to 5.0 except for 2S mode. $U_R^* = 5.0$ has C(2S) mode in Fig. 7(e) which is similar to 2S mode but vortices coalesce in the wake behind the solid body. When $U_R^* = 5.5$, it back to the 2S mode in the flow pattern, two single vortices are formed in each cycle and released from the cylinder. In the above-mentioned, vortex shedding is suppressed given that the cylinder adjacent to a plane boundary leads to the disappearance of vortex under the cylinder. With the influence of a plane boundary, the mode of vortex shedding behind cylinder is apparently different from that in uniform flow [9]. In summarize, this bigger separation bubble from the cylinder is strong enough to damage the shear layer of boundary as U_R^* ascends. Current wake patterns are consistent with the numerical investigations of the vortex shedding modes by Zhao and Cheng [10].

Figure 8 shows the trajectory diagrams of the movement of cylinder with the effect of the plane boundary. The movement of the cylinder is obviously different from that in uniform flow [9]. When U_R^* ranges from 5.5 to 7.0, the eight-shaped motion does not occur. The current movement of a cylinder is in an oval-shaped motion but nearly round because of the increasing oscillation amplitudes in the in-line direction. The single clockwise vortex street behind cylinder causes the clockwise periodic orbit of the movement of cylinder. The results mentioned above agrees with the experimenttal data of the effect on the plane boundary by Tsahalis [27]. Furthermore, it is noticed that the movement of cylinder is deflected with an angle as U_R^* increases for $e = 0.6$ but somehow it reverses the principle axis direction at $U_R^* = 8.5$. Similarly, this deflected and reverse phenomenon also exist for $e = 0.8$ but it occurs earlier than $e = 0.6$. The same phenomenon can also be observed when $e = 1.25$. Except for the case with small gap ratio, this phenomenon seems to occur earlier as the gap ratio increases. Unlike the other case mentioned above, the case with $e = 0.35$ did not reverse the principle axis direction at any U_R^*. The possible reason for this phenomenon is that the vortex shedding was suppressed at $e \leq 0.3$ [24, 25].

3.3 Effects of Reduced Velocity and Gap Ratio on the Cylinder Response

Variations of X_{max} and Y_{max} of a vibrating cylinder with respect to e and U_R^* are shown in Fig. 9. According to the amplitude response, it indicates that the jump behavior is found in the high end of the lock-in region. The figure also shows that there are distinct difference among all of the cases of e. For $e = 0.35$, the maximum amplitude in the in-line and the transverse direction is around 0.091D and 0.24D respectively at $U_R^* = 11.5$ Whereas for $e = 0.6$, the peak variation amplitude in the in-line and the transverse direction is around 0.0825D and 0.47D respectively at $U_R^* = 8.1$ Similarly, $e = 0.8$, the peak variation amplitude in the in-line and the transverse direction is around almost 0.08D and 0.50D respectively at $U_R^* = 6.7$. And, for $e = 1.25$, the maximum amplitude in the in-line and the transverse direction is around 0.057D and 0.55D respectively at $U_R^* = 5.4$. The maximum in-line oscillation amplitudes decrease gradually as e increases with the effect of a plane boundary. On the other hand, it is noted that the peak amplitude in the transverse direction increase gradually with increasing e due to the reducing effect of the boundary layer. Present study indicates that the vibration amplitudes in both directions grow upward and attain the peak amplitude slowly as U_R^* ascends, and descends quickly after critical values of U_R^* when the effect of boundary be-

Downloaded from https://www.cambridge.org/core. National Taiwan University Library, on 15 May 2018 at 01:02:41, subject to the Cambridge Core terms of use, available at https://www.cambridge.org/core/terms. https://doi.org/10.1017/jmech.2017.55

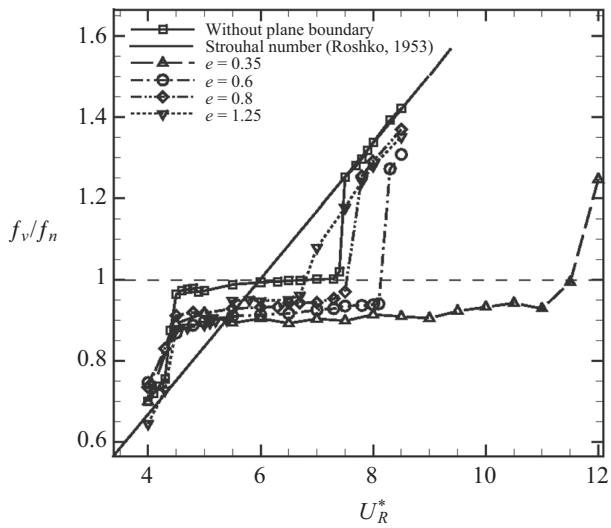

Fig. 10 Variation of the frequency ratio with different gap ratios and reduced velocities. The Strouhal number proposed by Williamson and Roshko [26] is defined by $St = 0.212(1 - 21.2/Re)$.

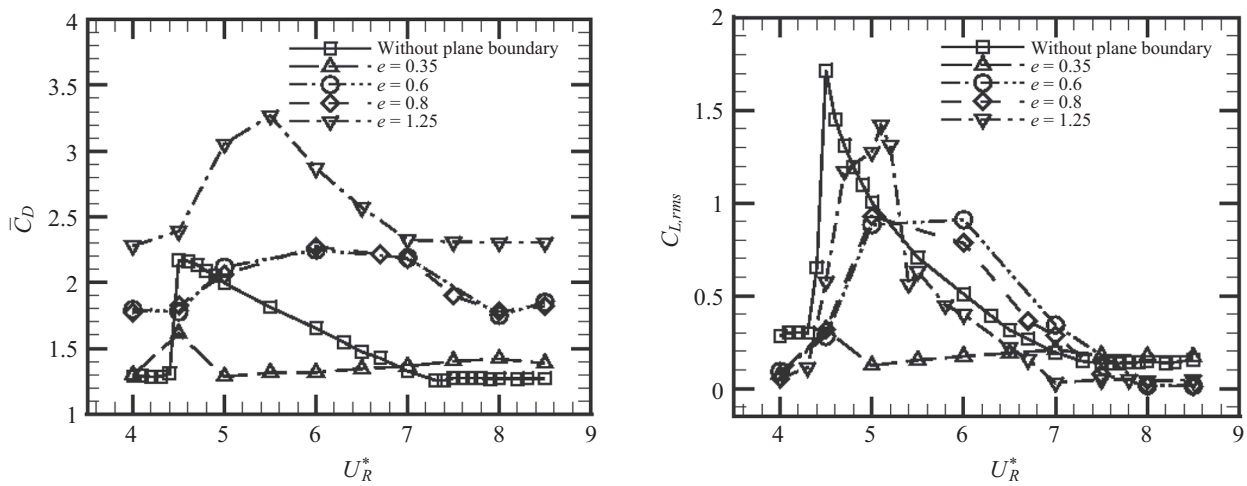

Fig. 11 Variation of the mean drag and r.m.s. values of lift coefficients of the vibrating cylinder with a variety of gap ratios and reduced velocities.

comes greater. The results are similar to the experimental investigation by Yang *et al.* [5]. Figure 10 reveals the corresponding frequency ratio between the vortex shedding and natural vibration frequencies for e = 0.35, 0.6, 0.8 and 1.25. The lock-in region is completely different in comparison with the Chern *et al.* [9] without the effect of the plane boundary (see Fig. 10). The ranges of U_R^* for lock-in region when e = 0.35, 0.6, 0.8 and 1.25 are about $4.5 \leq U_R^* \leq 11$, $4.5 \leq U_R^* \leq 8.1$, $4.5 \leq U_R^* \leq 7.5$ and $4.5 \leq U_R^* \leq 6.7$, respectively. The cylinder exhibits larger oscillation amplitudes and high aerodynamic forces within the lock-in region. Figure 10 shows that the frequency ratios are 0.88, 0.91, 0.93 and 0.95 for e = 0.35, 0.6, 0.8 and 1.25, respectively. The frequency ratio slightly decreases as the gap ratio decreases. The reason for the vortex shedding frequency does not match with the natural frequency of structure in the lock-in region could be that the only single vortex is shedding behind the cylinder. Although the range of U_R^* of lock-in region for e = 0.35, 0.6, 0.8 and 1.25 and without the boundary effect are different, it is found that the length of interval of lock-in region are almost same.

Figure 11 shows the variation of $\bar{C}_D$ and $C_{L,rms}$ of a vibrating cylinder with respect to e and increasing U_R^*. The results also shows the jump behavior at the high end of the lock-in region. Moreover, the behavior of C_L is related to the mode of vortex shedding, and it can be clearly seen for the variation of e. Although, the time-averaged coefficient oscillates about zero in a periodic manner. However, the calculated time-averaged drag and root-mean-square lift coefficient results, compared to a stationary cylinder at Re = 100, $\bar{C}_D$ and $C_{L,rms}$ for out of the lock-in region are nearly 1.30 and

Downloaded from https://www.cambridge.org/core. National Taiwan University Library, on 15 May 2018 at 01:02:41, subject to the Cambridge Core terms of use, available at https://www.cambridge.org/core/terms. https://doi.org/10.1017/jmech.2017.55

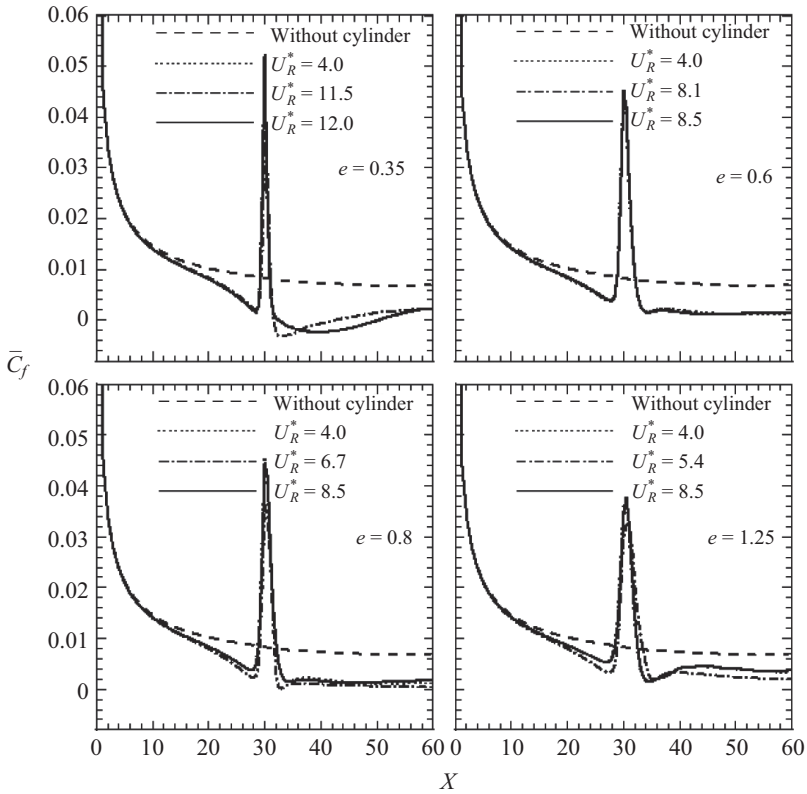

Fig. 12 The skin-friction drag on the spatial distribution of a plane boundary.

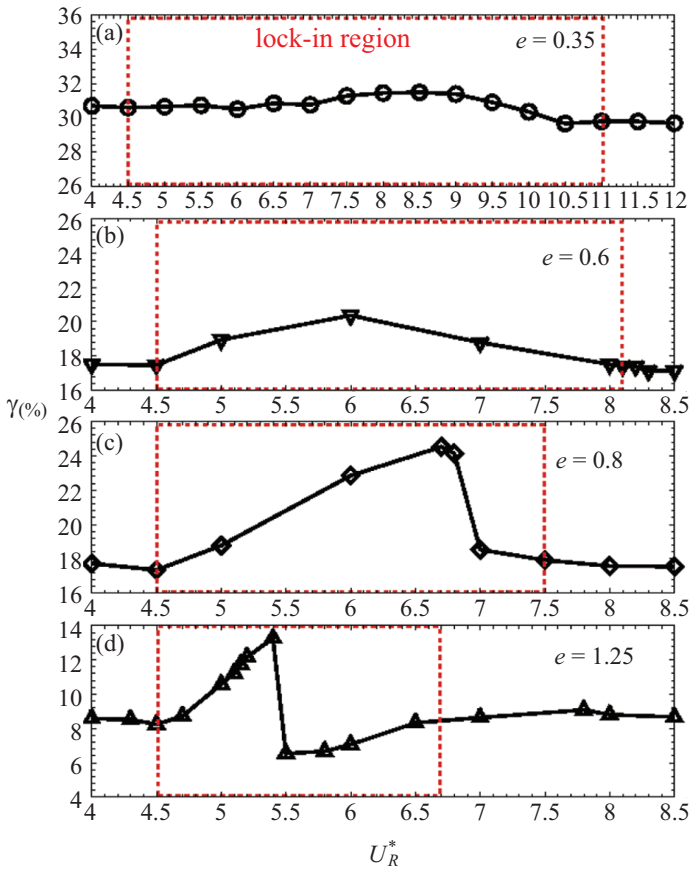

Fig. 13 The skin-friction drag reduction varies with the reduced velocity in various gap ratios.

Downloaded from https://www.cambridge.org/core. National Taiwan University Library, on 15 May 2018 at 01:02:41, subject to the Cambridge Core terms of use, available at https://www.cambridge.org/core/terms. https://doi.org/10.1017/jmech.2017.55

0.20 for e = 0.35 and for without the plane boundary, whereas, for e = 0.6 and 0.8 is nearly 1.80 and 0.10 respectively. Furthermore, it is found that beyond the lock-in region, the cylinder exhibits a small oscillation amplitude. Meanwhile, in the lock-in region, the cylinder experiences a large amplitude oscillation and high aerodynamic forces.

3.4 Skin-Friction Drag Reduction

Figure 12 shows that the mechanism of VIV disturbs the viscous flow on a plane boundary and the total skin-friction drag is decreased because of vortex shedding. Although the local skin-friction drag around the cylinder obviously increase, but the total skin-friction drag, the area under the local skin-friction drag curve, decrease before and behind the cylinder. In summary, the total skin-friction drag on a plane boundary is lower than the case without the cylinder. As shown in Figs. 13(b)-(d), the cylinder orbits, the oval-shaped motion in the lock-in region, γ has significant variation around at peak amplitude of vibrations except for e = 0.35 in Fig. 13(a). The possible reason is that the effect of boundary on cylinder is stronger when e decreases. Amplitude of transverse vibrations was suppressed which is difficult to disturb the shear layer behind a cylinder. On the other hand, it seems to be static circular cylinder, so that, do not change with U_R^* outside the lock-in region.

4. CONCLUSIONS

Two-degree-of-freedom vortex-induced vibration (VIV) of an elastically mounted circular cylinder close to a plane boundary is simulated numerically by using the direct-forcing immersed boundary (DFIB) method.

For two-degree-of-freedom VIV of the cylinder without the boundary effect, the peak oscillation amplitudes in both directions appear on the onset of lock-in/synchronization region. It is found that the amplitude response in the transverse direction is significantly higher than those of the in-line directions. The improvements of skin-friction drag are closely related to the modulation of surface flow, which is caused by the vibration induced velocity fluctuated on the boundary layer. While the effect of boundary layer is considered into two-degree-of-freedom VIV, the peak vibration amplitudes in the in-line and transverse directions as compared with the effect of a plane boundary are increased and decreased, respectively. From the initial amplitude response, the vibration amplitudes in both directions grow upward and reach the peak amplitude slowly as U_R^* ascends and in the final stage, it descends immediately. It leads to the result that the jump behavior is found at the high end of the lock-in region. With the effect of plane boundary, the wake structure analysis exhibits that the single clockwise vortex shedding dominates the wake process rather than the 2S and the C(2S) modes. In the lock-in region, the cylinder moves with a nearly round oval-shaped motion rather than the slightly oval-shaped motion due to the increasing oscillation amplitudes in the in-line direction. When the cylinder moves toward the plane boundary, the movement of cylinder shows that it leads to an inclined movement in the opposite direction. When it comes to the frequency response, the vortex shedding frequency does not match with the natural frequency of structure in the lock-in region since that only the single clockwise vortex shedding is found behind the cylinder. On the other hand, it also indicates that the frequency ratio of the lock-in region would rise when the cylinder is farther away from a plane boundary. The skin-friction drag of the surface was measured where a cylinder adjacent to a plane boundary. In the case of a cylinder placed adjacent to a plane boundary, vortex shedding appears behind the cylinder when the flow past it. Results show that this mechanism of VIV can achieve the effect of drag reduction by controlling boundary layer flow.

ACKNOWLEDGEMENTS

The authors would like to express their gratitude for the financial support from Ministry of Science and Technology, Taiwan (Grant No: MOST 103-2212-E-011-110-MY3 and MOST 104-2511-S-011-005-MY3).

NOMENCLATURE

English Symbols

c	structural damping, N.s.m^{-1};
$\overline{C}_D$	dimensionless time average in-line force coefficient;
$C_{L,rms}$	dimensionless root-mean-square transverse force coefficient;
$\overline{C}_f$	dimensionless time average skin-friction coefficient;
$\overline{C}_F$	dimensionless skin-friction drag coefficient;
$\overline{C}_{F_0}$	dimensionless skin-friction drag of a plane boundary without cylinder;
D	diameter of cylinder, m;
e	gap width between the plane boundary and the cylinder, m;
D	convergence criterion;
$\mathbf{f}^*$	dimensionless virtual force per unit mass;
f_n	natural frequency of structure, s^{-1};
f_v	frequency of vortex shedding, s^{-1};
R_x	dimensional resultant drag;
R_y	dimensional resultant lift;
f_n^*	dimensionless natural frequency of structure;
f_v^*	dimensionless frequency of vortex shedding;
$\mathbf{F}$	total dimensionless virtual force;
I,J	numbers of grid points in the x- and y-directions;

Downloaded from https://www.cambridge.org/core. National Taiwan University Library, on 15 May 2018 at 01:02:41, subject to the Cambridge Core terms of use, available at https://www.cambridge.org/core/terms. https://doi.org/10.1017/jmech.2017.55

k	structural stiffness, N.m^{-1};
L	length of plane boundary, m;
m^*	dimensionless mass ratio;
m_s	structural mass of solid, kg;
p	dimensionless pressure;
Re	Reynolds number, $u_\infty D/\nu$;
St	Strouhal number, $f_v D/u_\infty$;
t	time, s;
t^*	dimensionless time, tu_∞/D;
T	dimensionless time of the cylinder run in a cycle;
τ_w	shear stress at the surface of a plane boundary, $u\frac{du}{dy}$;
$\mathbf{u}$	dimensionless velocity of fluid;
$\mathbf{u}'$	dimensionless first intermediate velocity;
$\mathbf{u}''$	dimensionless second intermediate velocity;
$\mathbf{u}_s$	dimensionless velocity of solid;
u_∞	free stream velocity, m.s^{-1};
U_R^*	dimensionless reduced velocity, $u_\infty/(f_n D)$;
x,y	horizontal and vertical Cartesian coordinates;
X,Y	dimensionless displacements in the in-line and the transverse direction;

Greek Symbols

γ	dimensionless skin-friction drag reduction;
δ	thickness of the boundary layer, m;
ζ	dimensionless damping ratio of structure;
η	fraction of volume of solid in a cell;
μ	dynamic viscosity of fluid, N.s.m^{-2};
ν	kinematic viscosity of fluid, m^2.s^{-1};
ξ	refinement of sub-grids;
ρ	density, kg·m^{-3};
Ω	domain;

Subscripts

f	fluid;
s	solid;
rms	root-mean-square
i, j, k, l	numerical cell indices

Superscripts

n	time step level;
*	dimensionless parameter;
′	first intermediate time step level;
″	second intermediate time step level;

REFERENCES

1. Gad-el-Hak, M., *Flow Control: Passive, Active, and Reactive Flow Management*, Cambridge University Press, Cambridge (2000).
2. Strykowski, P. J. and Sreenivasan, K. R., "On the Formation and Suppression of Vortex Shedding at Low Reynolds Numbers," *Journal of Fluid Mechanics*, **218**, pp. 71-107 (1990).
3. Igarashi, T., "Drag Reduction of a Square Prism by Flow Control Using a Small Rod," *Journal of Wind Engineering and Industrial Aerodynamics*, **69-71**, pp. 141-153 (1997).
4. Huang, R. F. and Mao, S. W., "Separation Control on a Cantilever Wing with a Self-Excited Vibrating Rod," *Journal of Aircraft*, **39**, pp. 609-615 (2002).
5. Yang, B., Gao, F., Jeng, D. S. and Wu, Y., "Experimental Study of Vortex-Induced Vibrations of a Cylinder Near a Rigid Plane Boundary in Steady Flow," *Acta Mechanica Sinica*, **25**, pp. 51-63 (2009).
6. Singh, S. P. and Mittal, S., "Vortex-Induced Oscillations at Low Reynolds Numbers: Hysteresis and Vortex-Shedding Modes," *Journal of Fluids and Structures*, **20**, pp. 1085-1104 (2005).
7. Dettmer, W. and Perić, D., "A Computational Framework for Fluid Rigid Body Interaction: Finite Element Formulation and Applications," *Computer Methods in Applied Mechanics and Engineering*, **195**, pp. 1633-1666 (2006).
8. Du, L., Jing, X. and Sun, X., "Modes of Vortex Formation and Transition to Three Dimensionality in the Wake of a Freely Vibrating Cylinder," *Journal of Fluids and Structures*, **49**, pp. 554-573 (2014).
9. Chern, M. J., Kuan, Y. H., Nugroho, G., Lu, G. T. and Horng, T. L., "Direct-Forcing Immersed Boundary Modeling of Vortex-Induced Vibration of a Circular Cylinder," *Journal of Wind Engineering & Industrial Aerodynamics*, **134**, pp. 109-121 (2014).
10. Zhao, M. and Cheng, L., "Numerical Simulation of Two-Degree-of-Freedom Vortex-Induced Vibration of a Circular Cylinder Adjacent to a Plane Boundary," *Journal of Fluids and Structures*, **27**, pp. 1097-1110 (2011).
11. Sotiropoulos, F. and Yang, X., "Immersed Boundary Methods for Simulating Fluid-Structure Interaction," *Journal of Computational Physics*, **65**, pp. 1-21 (2014).
12. Yang, J. and Stern, F., "A Simple and Efficient Direct-Forcing Immersed Boundary Framework for Fluid-Structure Interactions," *Journal of Computational Physics*, **231**, pp. 5029-5061 (2012).
13. Mohd. Yusof, J., "Interaction of Massive Particles with Turbulence," Ph.D. Dissertation, Cornell University, U.S.A. (1996).
14. Noor, D. Z., Chern, M. J. and Horng, T. L., "An Immersed Boundary Method to Solve Fluid-Solid Interaction Problems," *Computational Mechanics*, **44**, pp. 447-453 (2009).
15. Chern, M. J., Shiu, W. C. and Horng, T. L., "Immersed Boundary Modeling for Interaction of Oscillatory Flow with Cylinder Array under Effects of Flow Direction and Cylinder Arrangement," *Journal of Fluids and Structures*, **43**, pp. 325-346 (2013).
16. Uhlmann, M., "An Immersed Boundary Method with Direct Forcing for the Simulation of Particulate Flows," *Journal of Computational Physics*, **209**, pp. 448-476 (2005).
17. Kempe, T. and Fröhlich, J., "An Improved Immersed Boundary Method with Direct Forcing for the Simulation of Particle Laden Flows," *Journal of*

Downloaded from https://www.cambridge.org/core. National Taiwan University Library, on 15 May 2018 at 01:02:41, subject to the Cambridge Core terms of use, available at https://www.cambridge.org/core/terms. https://doi.org/10.1017/jmech.2017.55

Computational Physics, **231**, pp. 3663-3684 (2012).

18. Wang, S. and Zhang, X., "An Immersed Boundary Method Based on Discrete Stream Function Formulation for Two- and Three-Dimensional Incompressible Flows," *Journal of Computational Physics*, **230**, pp. 3479-3499 (2011).
19. Deng, J., Shao, X. M. and Ren, A. L., "A New Modification of the Immersed-Boundary Method for Simulating Flows with Complex Moving Boundaries," *International Journal for Numerical Methods in Fluids*, **52**, pp. 1195-1213 (2006).
20. Peskin, C. S., "Flow Patterns around Heart Valves: A Numerical Method," *Journal of Computational Physics*, **10**, pp. 252-271 (1972).
21. Leonard, B. P., "A Stable and Accurate Convective Modelling Procedure Based on Quadratic Upstream Interpolation," *Computer Methods in Applied Mechanics and Engineering*, **19**, pp. 59-98 (1979).
22. Hirt, C., Nickols, B. and Romero, N., "*A Numerical Solution Algorithm for Transient Fluid LA-5852*," Los Alamos Scientific Laboratory, Los Alamos, New Mexico, U.S.A. (1975).
23. Leontini, J. S., Thompson, M. C. and Hourigan, K., "The Beginning of Branching Behavior of Vortex-Induced Vibration during Two-Dimensional Flow," *Journal of Fluids and Structures*, **22**, pp. 857-864 (2006).
24. Bearman, P. W. and Zdravkovich, M. M., "Flow around a Circular Cylinder Near a Plane Boundary," *Journal of Fluid Mechanics*, **109**, pp. 33-48 (1978).
25. Lei, C., Cheng, L. and Kavanagh, K. "Re-Examination of Effect of a Plane Boundary on Forces and Vortex Shedding of a Circular Cylinder," *Journal of Wind Engineering and Industrial Aerodynamics*, **80**, pp. 263-286 (1999).
26. Williamson, C. H. K. and Roshko, A., "Vortex Formation in the Wake of an Oscillating Cylinder," *Journal of Fluids and Structures*, **2**, pp. 355-381 (1988).
27. Tsahalis, D. T., "Vortex-Induced Vibrations of a Flexible Cylinder Near a Plane Boundary Exposed to Steady and Wave-Induced Currents," *Journal of Energy Resources Technology*, **106**, pp. 206-213 (1984).

(Manuscript received January 3, 2017,
accepted for publication June 8, 2017.)

Downloaded from https://www.cambridge.org/core. National Taiwan University Library, on 15 May 2018 at 01:02:41, subject to the Cambridge Core terms of use, available at https://www.cambridge.org/core/terms. https://doi.org/10.1017/jmech.2017.55